

Enhancing pretraining efficiency for medical image segmentation via transferability metrics

Gábor Hidy[†], Bence Bakos^{†,*}, András Lukács[†]

[†]*Eötvös Loránd University, Institute of Mathematics, Pázmány P. stny.
1/c, Budapest, H-1117, , Hungary*

Abstract

In medical image segmentation tasks, the scarcity of labeled training data poses a significant challenge when training deep neural networks. When using U-Net-style architectures, it is common practice to address this problem by pretraining the encoder part on a large general-purpose dataset like ImageNet. However, these methods are resource-intensive and do not guarantee improved performance on the downstream task. In this paper we investigate a variety of training setups on medical image segmentation datasets, using ImageNet-pretrained models. By examining over 300 combinations of models, datasets, and training methods, we find that shorter pretraining often leads to better results on the downstream task, providing additional proof to the well-known fact that the accuracy of the model on ImageNet is a poor indicator for downstream performance. As our main contribution, we introduce a novel transferability metric, based on contrastive learning, that measures how robustly a pretrained model is able to represent the target data. In contrast to other transferability scores, our method is applicable to the case of transferring from ImageNet classification to medical image segmentation. We apply our robustness score by measuring it throughout the pretraining phase to indicate when the model weights are optimal for downstream transfer. This reduces pretraining time and improves results on the target task.[‡]

Keywords: transferability, transfer learning, medical image segmentation,

*Corresponding author (bakosbence@student.elte.hu)

[‡]Code and results are available at <https://github.com/aielte-research/MedSegPretrainImageNet/>.

1. Introduction

Transfer learning concerns the practice of training a neural network on a large dataset, in order to utilize the learned representation to enhance performance on a smaller downstream dataset. This is done by taking the learned weights of the pretrained network and using them to initialize a model for the target task. The idea behind this process is that the model can learn basic low-level features from the large pretraining dataset, that are relevant for the downstream task as well. Transfer learning regularly leads to faster convergence speed and improved performance on the target task.

Traditionally, pretraining is conducted until convergence in some metric regarding only the pretraining task. However, overlong pretraining can lead to learning dataset- and task-specific features, which can compromise the generalization capabilities of the model. This creates the need for a method to find the optimal amount of pretraining that does not impair downstream performance.

In the field of medical image segmentation, the scarcity of high-quality labeled training data is a well-known issue. Thus pretraining neural networks on large datasets like ImageNet to then use them as a building block in the segmentation model is a common practice. Pretraining is often helpful in this domain, but overtraining on the source data is also a present danger. An example of two different configurations can be seen in Figure 1 for an instance where full pretraining, and another one where less ImageNet training provides optimal weights. Alternative evaluation methods for pretraining and transfer learning procedures have appeared in recent years, in the form of transferability metrics, but their applicability in this domain is limited.

In this paper, we present a novel method for model evaluation during the pretraining phase and two ways of its application. Our method applies techniques from contrastive learning using some desired invariances of the downstream task. We define a notion of robustness that measures how well a pretrained model represents the downstream dataset. We use this robustness as an indicator for the optimal pretraining length and show that accordingly timed pretraining leads to better downstream performance than either training from scratch or full pretraining. We also present a variation of the same method that significantly decreases pretraining time – often the most cost-

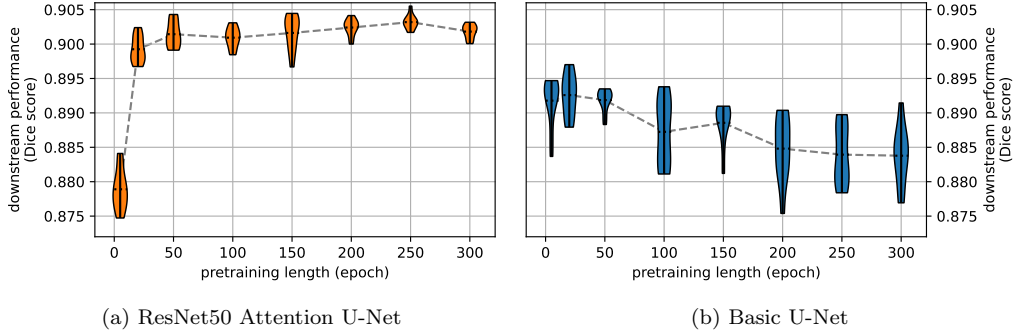


Figure 1: Two examples of ImageNet pretraining length influencing downstream performance. Models were trained on the ACDC dataset [1], with the encoder weights frozen after pretraining on ImageNet. At each encoder checkpoint, statistics from five downstream trainings are shown.

intensive part of training –, while still performing marginally better than a full ImageNet pretraining.

Our research contributes to the study of transferability in two major ways. First, we investigate a rarely studied aspect of transfer learning, namely the optimal length of ImageNet pretraining. Second, we focus on segmentation in the medical image domain, coupled with a source task of image classification. Other, commonly used transferability metrics are not applicable for this source–target task pair, even though the low amount of data in the target domain often necessitates such transfer.

The rest of this paper is structured as follows. Section 2 provides an overview of previous works concerning pretraining in medical image segmentation, and transferability metrics. In Section 3, the problem we set out to solve is formulated, and necessary definitions are given. Section 4 provides details about our proposed robustness-based transferability indicator. In Section 5, details of our experiments are presented. Section 6 contains our results. Finally, in Section 7 the importance of the different details of the methods used is investigated, while Section 8 discusses the limitations of our method.

2. Related Work

2.1. Pretraining for Medical Image Segmentation

To overcome the scarcity of labeled training data, extensive research has been conducted in the field of medical image segmentation. Weakly- and

unsupervised methods can eliminate the need for annotations [2, 3], while pretraining some part of the model architecture makes it possible to utilize data from outside of the downstream task.

Supervised classification on ImageNet [4] is one of the most common pretraining practices. However, several authors have voiced criticisms, contesting its effectiveness [5], and arguing for in-domain pretraining instead [6, 7]. Regardless, supervised ImageNet pretraining remains a popular transfer learning method to this day, due to the huge amount of publicly available trained models, and the fact that large medical image datasets for pretraining are less accessible.

2.2. Transferability Metrics

Transferability metrics for task and domain shift in deep learning has been a popular topic in recent years. In [8] a hypergraph is computed on a set of vision tasks in order to predict the performance of any transfer policy between them. LEEP [9] uses the pretrained model to create pseudolabels for the target task and measures the log-likelihood of the target labels based on them. \mathcal{N} LEEP [10] extends this idea by clustering extracted features instead of predicted labels, thus enabling the use of the metric for unsupervised pretraining scenarios. LogME [11] estimates the compatibility of target labels and features extracted by the pretrained network. DEPARA [12] selects both model weights and a corresponding embedding space by building a dense graph of inputs, where edges are weighted based on relatedness.

These metrics all seem to work well in certain scenarios, but – as has been observed in [13] – there is no one method that is clearly superior in all cases. Moreover, in [14] these metrics are found to be even less reliable in the medical image domain. Another limitation is that each of them requires a target task that is either regression or classification, and thus cannot be applied when transferring from a classification task to semantic segmentation.

3. Background

3.1. U-Net-Style Models

Medical image segmentation tasks often make use of U-shaped models with lateral skip connections. This style of architecture was first used by Ronneberger *et al.* in [15]. We therefore refer to these models as U-Net-style architectures.

U-Net and its descendant models are encoder–decoder structures. The **encoder** is a classical image processing network. It can be structured into several **levels**, where the spatial size and number of channels are constant within one level and change across levels, by decreasing the spatial dimensions and increasing the number of channels. The **decoder** has a similar structure, but with the spatial size increasing and the number of channels decreasing across levels. Lateral skip connections connect the corresponding levels of the encoder and decoder.

Since the encoder part of these models can be used as the backbone of an image classification network, a common way to pretrain U-Net-style models is to train the encoder – together with a small classification head – on a classification task, and then use these pretrained weights, together with randomly initialized decoder weights, to transfer to the target domain.

3.2. Notations Related to Transferability

Here we define the notation regarding transferability used throughout this paper. A **task** is defined as a triplet $\mathcal{X} = (X, L, f^*)$, where X is a dataset, L is the possible set of labels for all datapoints, and $f^* : X \rightarrow L$ is the ground truth labeling function. A **model** for \mathcal{X} is a function $f : X \rightarrow L$ approximating f^* . A **metric** $m_{\mathcal{X}}$ on \mathcal{X} is a function that maps models to real numbers (scores).

Consider a source task \mathcal{S} , and a target (downstream) task \mathcal{T} with evaluation metric $m_{\mathcal{T}}$. We assume that obtaining a model with good performance on \mathcal{S} is straightforward, while doing so on \mathcal{T} is harder. Furthermore, we also assume that for each model f for \mathcal{S} , we can derive a model f' for \mathcal{T} . Therefore, we want to find a model with good $m_{\mathcal{T}}$ -performance by first obtaining a model f on \mathcal{S} and then deriving f' for \mathcal{T} . In the case of this paper, this will consist of pretraining a segmentation model encoder on the source task to get f , and using these weights to initialize the model, then fine-tuning on the segmentation task to get f' .

When discussing transferability, we consider a family of models $\{f_{\vartheta}\}_{\vartheta \in \Theta}$ for \mathcal{S} , indexed by elements of a finite set Θ . The goal is to find $\vartheta \in \Theta$ such that the downstream performance $m_{\mathcal{T}}(f'_{\vartheta})$ is optimal. For this we are looking for a **transferability indicator** $\varrho_{\mathcal{S}, \mathcal{T}}(f_{\vartheta})$, and define an associated **transferability indicator score** (TIS) of $\varrho_{\mathcal{S}, \mathcal{T}}$ on Θ as

$$\text{TIS}(\varrho_{\mathcal{S}, \mathcal{T}}, \Theta) = \frac{m_{\mathcal{T}}(f'_{\vartheta^*})}{\max_{\vartheta \in \Theta} (m_{\mathcal{T}}(f'_{\vartheta}))}, \quad (1)$$

where

$$\vartheta^* = \operatorname{argmax}_{\vartheta \in \Theta} (\varrho_{\mathcal{S}, \mathcal{T}}(f_{\vartheta})).$$

This score measures the relative downstream performance of the model chosen based on $\varrho_{\mathcal{S}, \mathcal{T}}$ to the best performing downstream model. It reaches 1 when $\varrho_{\mathcal{S}, \mathcal{T}}$ predicts the highest score for the model with the best $m_{\mathcal{T}}$ -performance.

3.3. Contrastive Learning

Contrastive methods – first appearing in [16] – aim to train a model to represent the structure inherent to a dataset, without comparing its output to a set of labels in a supervised manner. Instead, the task is to distinguish between related and unrelated pairs of datapoints. Due to its usefulness in self-supervised learning, this approach has grown really popular in recent years. A common contrastive learning method is to use a triplet loss function [17], which takes triplets of queries, positive keys, and negative keys, denoted by q , k^+ , and k^- respectively. Similar representations of q and k^+ are rewarded, as well as distinct representations of q and k^- . The triplet loss is defined as

$$\mathcal{L}_{\text{triplet}}(f) = \mathbb{E}_{q, k^+, k^-} \left[\max(0, d(f(q), f(k^+)) - d(f(q), f(k^-)) + \varepsilon) \right], \quad (2)$$

where d is a distance measure, and $\varepsilon > 0$ is a margin parameter.

4. Measuring Transferability Across Encoder Checkpoints

Further on, we restrict ourselves to the case where the source task \mathcal{S} is classification on ImageNet, and the target task \mathcal{T} is a medical image segmentation problem, with the Dice index as the evaluation metric $m_{\mathcal{T}}$. Our direct goal is to provide a transferability indicator for the encoder weights at different steps during pretraining, thus avoiding overtraining, and potentially decreasing pretraining time.

Therefore we define Θ as a set of checkpoints, where f_{ϑ} is a model pre-trained on ImageNet for ϑ epochs. From a pretrained encoder f_{ϑ} , we obtain f'_{ϑ} by initializing the encoder weights of the segmentation model with the pretrained encoder backbone and then fine-tuning it on \mathcal{T} .

The choice of ϑ can have a significant effect on downstream performance $m_{\mathcal{T}}$, as seen in Subfigure 1a. However, using the accuracy on ImageNet as a transferability indicator is also ill-advised, as evidenced by Subfigure 1b.

Instead, we propose to use a contrastive learning inspired indicator $\varrho_{S,T}$, based on Equation 2. For each q_i target datapoint we obtain k_i^+ by applying a set of random augmentations for q_i , and let k_i^- be a randomly chosen and augmented other target datapoint. We define the **robustness** of the representation of model f_ϑ as

$$\varrho_{S,T}(f_\vartheta) = 1 - \frac{1}{|T|} \sum_{x_i \in T} \max \left(0, d(\hat{f}_\vartheta(\tilde{q}_i), \hat{f}_\vartheta(k_i^+)) - d(\hat{f}_\vartheta(\tilde{q}_i), \hat{f}_\vartheta(k_i^-)) + \varepsilon \right), \quad (3)$$

where T is the target dataset, d is a distance measure, \tilde{q} is an augmented version of q , and \hat{f}_ϑ obtains a representation by extracting it from an inner layer of f_ϑ . The precise choice of these parameters is discussed in Sections 6 and 7. Note that regardless the choice of the parameters, this metric can be applied to any source–target task pairs, including transferring from ImageNet classification to a downstream segmentation task.

We present two applications of the robustness defined above as a transferability indicator. Our first approach is to measure robustness at regular intervals during pretraining, and, in the end, use the weights corresponding to the highest score to transfer to the target task. This is an **offline** method, since best weights can still only be obtained after a full pretraining. We also suggest an **online** method, where the robustness score acts as an early stopping condition for pretraining. This approach potentially only finds local optima, thus providing less improvement in performance than the offline version, but prevents unnecessary pretraining steps.

5. Methodology

To show that robustness is a good transferability indicator, we tested its predictive power on several encoder–decoder models, pretraining schemes, target datasets, and downstream training methods. This section provides an overview of these variables.

5.1. Model Architectures

We experimented with three different segmentation model architectures. They were chosen because of their widespread use in medical image segmentation tasks, and because they serve as an accurate showcase of the variety of U-Net-style architectures, as they include both a fully convolutional and a fully transformer-based model, in addition to a model that makes use of both

convolutional layers and attention gates. Here we list our models, together with a basic description. Appendix A.1 describes each architecture in more detail.

The **basic U-Net** [15] architecture consists of a simple convolutional encoder and decoder, with identical lateral skip connections. **ResNet50 Attention U-Net** uses a ResNet50 [18] backbone as its encoder, and a simple convolutional network (without residual connections) as its decoder. Here instead of identical lateral skip connections, attention gates are used, as in the Attention U-Net [19] model. Finally, our third model, **Swin U-Net** [20], uses a Swin Transformer [21] as its encoder, and an analogous decoder also made out of Swin Transformer blocks.

5.2. Medical Image Datasets

We trained each of our segmentation models on three downstream datasets, chosen from three separate medical image domains, consisting of both multiclass and binary segmentation tasks.

The **ACDC** (Automated Cardiac Diagnosis Challenge) dataset [1] contains cardiac MRI images of a total of 150 patients. The processed dataset provides a 4D representation of the interval of the cardiac cycle. From this, we only used the end-diastolic (ED) and the end-systolic (ES) frame per case, since segmentation masks are only provided for these frames. On these masks, the right and left ventricular cavities, and the myocardium are annotated, resulting in a total of three classes (not counting the background). The same train–test split was used as in the original challenge, with 100 train and 50 test cases. The 3D frames were divided into approximately ten 2D slices each, which led to 1 902 train and 1 076 test images.

The **COVID-QU-Ex** dataset [22] consists of chest X-ray images from both healthy patients and people infected with COVID-19, or viral or bacterial pneumonia. We used the 2 913 image subset of this dataset that provides segmentation masks for the area of the lung infected with COVID-19, where each pixel is annotated as either infected or not. The official 583-image test was used, which left us with 2 330 training images.

The Indian Diabetic Retinopathy Image Dataset [23], or **IDRiD**, is a dataset consisting of retina scans, with labels related to diabetic retinopathy. It has around five hundred images with classification labels, and 81 images with segmentation masks for four different types of lesions – microaneurysms, hemorrhages, soft exudates, and hard exudates. For our experiments, we chose the microaneurysm masks to define a binary segmentation task. The

images were divided into 54 train and 27 test sources, following the split of the original challenge. Each image is 2848×4288 pixels, which was first resized to 1120×2240 , then the training and test slices were sampled from these. For testing, we simply partition the original image into 50 equal-sized slices, giving us 1350 test images. For training, 119 slices were randomly sampled from each frame in each epoch, giving us 6 426 training images per epoch.

For a more detailed description of the datasets and our preprocessing methods see Appendix A.2.

5.3. Pretraining the Encoders

We pretrained each of the three encoders for 300 epochs, using Adam [24], and cosine annealing learning rate scheduling [25] with linear warmup [26]. We used decoupled weight decay [27] and label smoothing [28] for regularization, as well as stochastic depth [29] for ResNet50 and the Swin Transformer. We trained each model twice, using two different training setups, that we dubbed “simple” and “advanced”. Here we provide an overview of each method. For more details, refer to Appendix A.3.

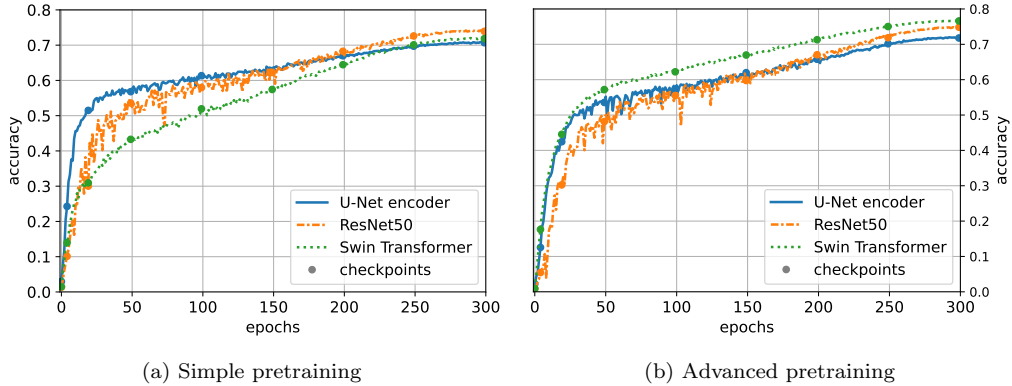


Figure 2: Progression of validation accuracies on ImageNet during training

For our **simple pretraining**, we used a five-epoch learning rate warmup for the U-Net encoder, and twenty epochs for the other two models. We used a base learning rate of 0.004 and a batch size of 4096 for all models. We only used random resizing, crops, and flips as augmentation during training.

Our **advanced pretraining** scheme is based on [30], following [21]. We followed the 1024 batch size for Swin Transformer, but we used a 4096 batch

size for the convolutional networks, following the training setup used for ConvNeXt [31]. We used a fixed batch size to learning rate ratio, so we trained the Swin Transformer with a learning rate of 0.001, and the convolutional models with 0.004. We used a twenty-epoch warmup for all models. RandAugment [32], mixup [33], CutMix [34], and random erasing [35] were used for augmentation.

Figure 2 shows the learning curves of each model. We saved the weights of each model after the 1st, 5th, 20th, 50th, 100th, 150th, 200th, 250th, and 300th epoch. Encoder weights were initialized from these checkpoints during downstream training.

5.4. Training the Segmentation Models

To train the segmentation models, we resized all images to 224×224 . Grayscale images were converted by using their singular grayscale channel for all three color channels. Random rotations and flips were used as augmentation, as well as randomly jittering the brightness, saturation, contrast, and hue values of colored images.

We trained for 150 epochs, using SGD with momentum 0.9 and weight decay 10^{-4} . The learning rate in the i^{th} iteration was $(1 - \frac{i}{N})^{0.9}$, where N is the total number of iterations. The learning rate was updated after each optimizer step. We trained with a version of the Dice loss [36], following [20].

For each model, we investigated both training the full model and training the decoder only. In the former case, we used the pretrained encoder weights only as weight initialization, while in the latter the frozen encoder served as a feature extractor. We report results with both of these methods.

With three models, three downstream datasets, two pretraining and two downstream training schemes, and ten encoder checkpoints, we considered over 300 configurations. We trained each configuration five times to obtain their mean performance, resulting in over 1500 experiments. Table 1 shows the best score of each model on each dataset. We provide a file with the results of each experiment in our GitHub repository.

Table 2 shows the relative difference between the worst and best performing initialization for each setup. When it is high (*e.g.*, when fully training a U-Net or ResNet50 Attention U-Net on ACDC), it means that the length of ImageNet pretraining – or lack thereof – makes no significant difference to the model. Configurations when this indicator is low mean that in that case, choosing the wrong checkpoint to start the downstream training would lead to a significant drop in performance.

	basic U-Net		R50 Atn. U-Net		Swin U-Net	
	full training	decoder only	full training	decoder only	full training	decoder only
ACDC	0.908	0.895	0.907	0.904	0.895	0.853
COVID-QU	0.846	0.829	0.853	0.844	0.835	0.827
IDRiD	0.486	0.483	0.494	0.488	0.494	0.464

Table 1: Best achieved scores (Dice indices) on each dataset, grouped by models

	basic U-Net		R50 Atn. U-Net		Swin U-Net	
	full training	decoder only	full training	decoder only	full training	decoder only
ACDC	0.992	0.975	0.991	0.935	0.902	0.801
COVID-QU	0.987	0.962	0.979	0.922	0.915	0.854
IDRiD	0.932	0.906	0.924	0.924	0.824	0.740

Table 2: Ratio of the downstream scores of the worst and best performing initialization on each dataset, grouped by models

6. Results

During our research we experimented with different choices of d , ε , \hat{f}_θ , and \tilde{q} in Equation 3. In Section 7, we provide a more detailed investigation of these parameters. In this section, we report the results with the variation that achieved the highest scores, in which we used the cosine distance

$$d(q, k) = 1 - \frac{\langle q, k \rangle}{\|q\| \|k\|} \quad (4)$$

for the distance metric when calculating the robustness, with a margin of $\varepsilon = 0.5$. We obtained \tilde{q} , k^+ , and k^- by applying random jittering to the hue, saturation, brightness, and contrast values. The representation $\hat{f}_\theta(\cdot)$ was taken from the second-to-last level of the encoder. When we were only planning to train the decoder, a pooled representation was taken; for full training, we did not pool.

We report the transferability indicator (or relative accuracy) scores – see Equation 1 – using the Dice index as the downstream evaluation metric. We compare the TIS of our robustness indicator to the two common-practice baselines: no pretraining, and performing a full pretraining on ImageNet.

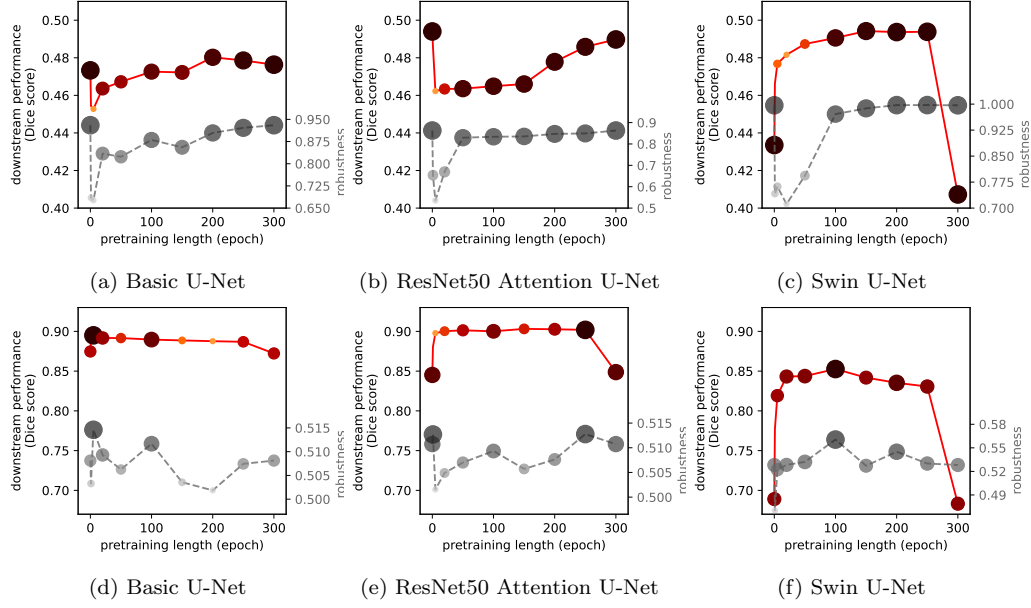


Figure 3: Robustness compared to performance on a downstream segmentation dataset. A larger and darker dot indicates higher robustness. Under each graph, the exact robustness scores are indicated by dashed gray lines. All encoders were pretrained using the “advanced” scheme. Subfigures (a)–(c) are fully trained on IDRiD. Subfigures (d)–(f) are trained on ACDC, with the encoder weights frozen during training.

(The latter can also be understood as using the ImageNet accuracy as a transferability indicator.)

Across all our setups, our robustness score produced a TIS of over 98% on average calculated offline, and over 97% calculated online. We report a worst-case performance of over 95% offline, and 91% online. As a comparison, both no pretraining and ImageNet pretraining can provide under 75% TIS. Even at its worst, our offline method shows a 0.006 absolute decrease in Dice index, or a 1.3% relative decrease, compared to full ImageNet pretraining.

Figure 3 shows examples of training setups with downstream performances and robustness indicated for each checkpoint. Note that offline robustness provides good predictions in various circumstances, including ones where downstream performance monotonically increases with pretraining time up to epoch 250 (Subfigure 3c), and ones where the clear optimum is at a much shorter, 100 epoch long pretraining (Subfigure 3f).

We note that randomly initialized encoders often provide really high ro-

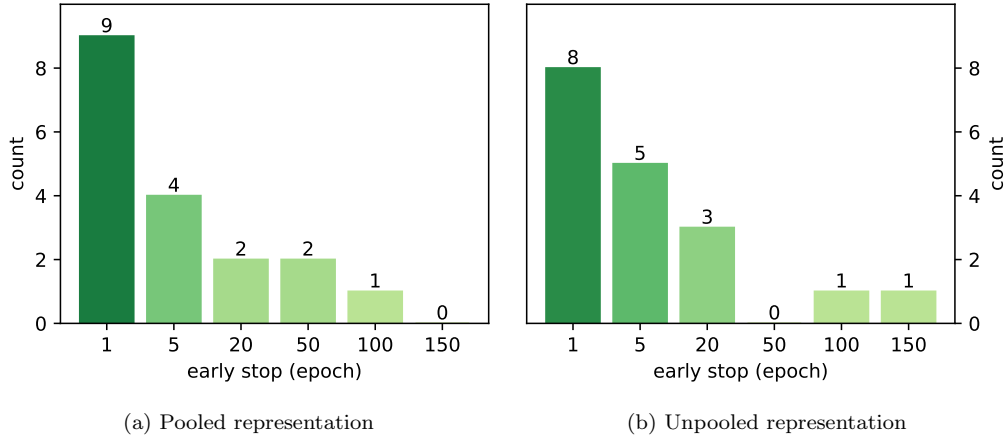


Figure 4: Counts of predicted best epoch indices, when using an online method

bustness scores, even when that does not correlate with a higher downstream performance. For this reason, we calculated online scores by disregarding the randomly initialized model, and only starting to calculate robustness after the first epoch. We find that using robustness as an online predictor provides similar results to always using a fully pretrained network – with only a fraction of the pretraining time –, and is almost always better than no pretraining.

Figure 4 shows how many times each epoch index was predicted as best in an online manner. Out of the 18 configurations (six ImageNet pretraining, each evaluated for three datasets), no online method would have trained for longer than 150 epochs (as opposed to the full ImageNet pretraining, which is 300 epochs), and most would have stopped after only one epoch – while still providing better initial weights than random initialization.

Table 3 shows our results, compared to full pretraining and no pretraining. For each model, we had three datasets and two pretraining schemes; we averaged these scores out over the model and pretraining scheme axis in Subtable 3a, and the dataset and pretraining schemes in Subtable 3b.

Certain dataset–model configurations tend to provide the same performance, regardless of encoder weights. With these setups, no major improvement is needed over training from scratch. In contrast, experiments run on IDRiD (which is the hardest dataset – see Table 1), or using Swin U-Net (which is the model where pretraining tends to have the largest impact – see Table 2) show that both a from-scratch initialization and a full pretraining

	ACDC		COVID-QU		IDRiD	
	full training	decoder only	full training	decoder only	full training	decoder only
robustness (offline)	0.989	0.999	0.996	0.986	0.991	0.984
robustness (online)	0.984	0.955	0.982	0.956	0.959	0.948
ImageNet accuracy	0.982	0.950	0.982	0.953	0.963	0.930
no pretraining	0.973	0.909	0.967	0.921	0.945	0.866

(a) Averaged over models and pretraining schemes

	basic U-Net		R50 Atn. U-Net		Swin U-Net	
	full training	decoder only	full training	decoder only	full training	decoder only
robustness (offline)	0.996	0.986	0.990	0.996	0.990	0.987
robustness (online)	0.978	0.985	0.989	0.953	0.958	0.921
ImageNet accuracy	0.998	0.969	0.989	0.963	0.940	0.900
no pretraining	0.994	0.958	0.990	0.929	0.901	0.809

(b) Averaged over datasets and pretraining schemes

Table 3: Comparison of the TIS of our robustness score, ImageNet accuracy, and simply training from scratch

can result in a significantly worse downstream performance than what could be achieved with the encoder weights initialized from the right checkpoint.

Table 4 shows only results on IDRiD, with the encoders pretrained using the advanced scheme. In that example, using full or no pretraining for Swin U-Net provides under 90% relative accuracy for the full training, and around 75% relative accuracy when only the encoder is trained; compared to that, robustness leads to an over 99% relative accuracy in both cases.

7. Ablation Studies

In this section, we investigate certain scenarios demonstrating the effect of the choice of d , ε , and $\hat{f}_\vartheta(\cdot)$ in Equation 3. We provide a more detailed analysis of the significance of these parameters in Appendix B.

7.1. Other Similarity Metrics

Besides the cosine distance, we investigated other distance metrics for d – namely the L^2 distance and the Pearson correlation coefficient. We

	basic U-Net		R50 Atn. U-Net		Swin U-Net	
	full training	decoder only	full training	decoder only	full training	decoder only
cosine distance	0.986	1.000	0.941	0.983	0.999	0.993
Pearson correlation	0.986	0.969	0.941	0.983	0.999	0.929
L^2 distance	0.943	0.977	0.938	0.953	0.965	0.975
ImageNet accuracy	0.992	0.910	0.991	0.924	0.824	0.748
no pretraining	0.986	0.941	1.000	0.926	0.877	0.758

Table 4: TIS of different distance metrics, measured on IDRiD. Encoders were pretrained using the “advanced” scheme

found that the cosine distance works consistently best across all examined datasets. The other two metrics also provided better transferability indicator scores than either the ImageNet accuracy or training from scratch. Table 4 shows the relative accuracies of each metric, on IDRiD, with the encoders pretrained using the advanced scheme.

7.2. Effect of the Margin Parameter

margin	basic U-Net		R50 Atn. U-Net		Swin U-Net	
	full training	decoder only	full training	decoder only	full training	decoder only
0.25	0.997	0.968	0.995	0.922	0.989	1.000
0.50	0.997	0.968	0.995	0.922	0.989	1.000
0.75	0.994	0.968	0.995	0.922	0.989	0.854
1.00	0.994	0.968	0.995	0.922	0.989	0.854

Table 5: TIS of different margins, measured on COVID-QU. Encoders were pretrained using the “advanced” scheme

We find that the margin parameter ε does not influence performance for the most part. Switching from 0.5 to 0.25 has practically no effect. Going above 0.5 leads to a slight average decrease, and rarely – *e.g.*, in the example shown in Table 5 – to a more significant decrease.

7.3. Choosing Encoder Representation

When using an encoder module as a feature extractor, it is natural to make use of the whole model – that is, use the output of the last layer as the

level	pooled	basic U-Net		R50 Atn. U-Net		Swin U-Net	
		full training	decoder only	full training	decoder only	full training	decoder only
last	yes	0.941	0.969	0.949	0.988	0.830	0.740
	no	0.999	1.000	0.994	0.925	0.830	0.740
second to last	yes	0.941	0.969	0.935	1.000	0.994	0.970
	no	0.999	1.000	0.960	0.972	1.000	0.998

Table 6: Transferability indicator scores when taking different representations. Models are trained on IDRiD. Encoders were pretrained using the “simple” scheme

embedding of the input. However, we found that using the last level instead of the second to last one leads to worse performance on average. We theorize this is because the last level learns dataset-specific features, which do not transform well to the downstream task.

Another question is whether or not to apply pooling over the spatial dimensions of the embedded image. We found that when the full model was trained on the downstream task, no pooling was slightly better, but when only the encoder was trained, it did not help the average performance. In this case, we reported our results with the use of pooling, as that would be preferable in practice, due to a lowered computational cost.

Table 6 shows an example setup, and compares different representations. We note that in many cases, the last level does not provide a significantly worse representation. However, in the case of Swin U-Net, it picks one of the worst possible checkpoints (compare to the worst-to-best ratios in Table 2), whereas taking the representation from the second to last layer provides a solid performance.

8. Limitations

The main limitation of our method is the fact that the robustness of a randomly initialized encoder is often bigger than that of a model pretrained for a few epochs, which presents a challenge when using robustness as an early stopping condition. In this paper, we elected to disregard randomly initialized weights, which lead to good average performance, but it also means that whenever no pretraining would lead to optimal downstream performance – which can happen –, our online method fails to recognize that. We note that this phenomenon can be counteracted by also training a segmentation

network from scratch, but this would require additional training time.

The online method is also generally worse than the offline method, indicating that it is prone to find local maxima. More generally, the Spearman correlation of robustness and downstream performance is relatively low, even if their optima coincide.

We also note that generally robustness is a better indicator when the encoder weights are not modified during training for the downstream task, but this setup also results in worse performance on average.

9. Conclusion

We propose a method to more efficiently pretrain encoders of U-Net-based architectures on ImageNet. Using a novel transferability indicator that measures the robustness of the target dataset representation to choose the optimal length of pretraining, we can significantly improve downstream performance. As an additional benefit, our method is applicable to models transferring from classification to segmentation, which is a property missing from other transferability metrics.

We also suggest a version of our method that decreases pretraining time by a factor anywhere between 2 and 300, while still providing slightly better expected downstream performance than full ImageNet pretraining, and even surpassing it significantly in certain scenarios.

This paper is concerned with a special case of a much more general problem present in many fields of deep learning. Our solution for this special case can in theory be used in other domains and modalities even outside computer vision. The presented results demonstrate the effectiveness of our method for medical image segmentation tasks. Assessing its performance outside of this scope should be subject to further research.

CRediT authorship contribution statement

Gábor Hidy: Conceptualization, Methodology, Software, Formal analysis, Investigation, Data Curation, Writing – Original Draft, Visualization.
Bence Bakos: Conceptualization, Methodology, Software, Formal analysis, Investigation, Data Curation, Writing – Original Draft. **András Lukács:** Conceptualization, Resources, Writing – Original Draft, Supervision, Project administration, Funding acquisition.

Acknowledgements

The research was supported by the Hungarian National Research, Development and Innovation Office within the framework of the Thematic Excellence Program 2021 – National Research Sub programme: “Artificial intelligence, large networks, data security: mathematical foundation and applications” and the Artificial Intelligence National Laboratory Program (MILAB), and the Hungarian National Excellence Grant 2018-1.2.1-NKP-00008.

We express our thanks to Thomas Kolb for his help with implementing the Swin Transformer and Swin U-Net models.

Declaration of Generative AI and AI-assisted technologies in the writing process

During the preparation of this work the authors used OpenAI’s ChatGPT in order to improve readability and language. After using this tool, the authors reviewed and edited the content as needed and take full responsibility for the content of the publication.

References

- [1] O. Bernard, A. Lalande, C. Zotti, F. Cervenansky, X. Yang, P.-A. Heng, I. Cetin, K. Lekadir, O. Camara, M. A. G. Ballester, et al., Deep learning techniques for automatic MRI cardiac multi-structures segmentation and diagnosis: is the problem solved?, *IEEE Transactions on Medical Imaging* 37 (2018) 2514–2525. doi:10.1109/TMI.2018.2837502.
- [2] H. Du, Q. Dong, Y. Xu, J. Liao, Weakly-supervised 3D medical image segmentation using geometric prior and contrastive similarity, *IEEE Transactions on Medical Imaging* 42 (2023) 2936–2947. doi:10.1109/TMI.2023.3269523.
- [3] C. Liu, M. Amodio, L. L. Shen, F. Gao, A. Avesta, S. Aneja, J. C. Wang, L. V. D. Priore, S. Krishnaswamy, CUTS: A framework for multigranular unsupervised medical image segmentation (October 2023). arXiv:2209.11359v6.

- [4] O. Russakovsky, J. Deng, H. Su, J. Krause, S. Satheesh, S. Ma, Z. Huang, A. Karpathy, A. Khosla, M. Bernstein, A. C. Berg, L. Fei-Fei, ImageNet Large Scale Visual Recognition Challenge, *International Journal of Computer Vision* 115 (2015) 211–252. doi:10.1007/s11263-015-0816-y.
- [5] K. He, R. Girshick, P. Dollár, Rethinking ImageNet pre-training, in: *Proceedings of the IEEE/CVF International Conference on Computer Vision (ICCV)*, Seoul, South Korea, 2019, pp. 4918–4927. doi:10.1109/ICCV.2019.00502.
- [6] A. Kalapos, B. Gyires-Tóth, Self-supervised pretraining for 2D medical image segmentation, in: *European Conference on Computer Vision*, Springer, Tel Aviv, Israel, 2022, pp. 472–484. doi:10.1007/978-3-031-25082-8_31.
- [7] Y. Wen, L. Chen, Y. Deng, C. Zhou, Rethinking pre-training on medical imaging, *Journal of Visual Communication and Image Representation* 78 (2021) 103145. doi:10.1016/j.jvcir.2021.103145.
- [8] A. R. Zamir, A. Sax, W. Shen, L. J. Guibas, J. Malik, S. Savarese, Taskonomy: Disentangling task transfer learning, in: *2018 IEEE/CVF Conference on Computer Vision and Pattern Recognition*, Salt Lake City, Utah, United States of America, 2018, pp. 3712–3722. doi:10.1109/CVPR.2018.00391.
- [9] C. Nguyen, T. Hassner, M. Seeger, C. Archambeau, LEEP: A new measure to evaluate transferability of learned representations, in: *Proceedings of the 37th International Conference on Machine Learning, Proceedings of Machine Learning Research*, 2020, pp. 7294–7305.
- [10] Y. Li, X. Jia, R. Sang, Y. Zhu, B. Green, L. Wang, B. Gong, Ranking neural checkpoints, in: *2021 IEEE/CVF Conference on Computer Vision and Pattern Recognition (CVPR)*, Nashville, Tennessee, United States of America, 2021, pp. 2662–2672. doi:10.1109/CVPR46437.2021.00269.
- [11] K. You, Y. Liu, J. Wang, M. Long, LogME: Practical assessment of pre-trained models for transfer learning, in: *Proceedings of the 38th*

International Conference on Machine Learning, Proceedings of Machine Learning Research, 2021, pp. 12133–12143.

- [12] J. Song, Y. Chen, J. Ye, X. Wang, C. Shen, F. Mao, M. Song, DE-PARA: Deep attribution graph for deep knowledge transferability, in: 2020 IEEE/CVF Conference on Computer Vision and Pattern Recognition (CVPR), Seattle, Washington, United States of America, 2020, pp. 3922–3930. doi:10.1109/CVPR42600.2020.00398.
- [13] A. Agostinelli, M. Pándy, J. Uijlings, T. Mensink, V. Ferrari, How stable are transferability metrics evaluations?, in: Computer Vision – ECCV 2022, Vol. 34, Tel Aviv, Israel, 2022, pp. 303–321. doi:10.1007/978-3-031-19830-4_18.
- [14] L. Chaves, A. Bissoto, E. Valle, S. Avila, The performance of transferability metrics does not translate to medical tasks, in: MICCAI Workshop on Domain Adaptation and Representation Transfer, Springer, 2023, pp. 105–114.
- [15] O. Ronneberger, P. Fischer, T. Brox, U-Net: Convolutional networks for biomedical image segmentation, in: Medical Image Computing and Computer-Assisted Intervention – MICCAI 2015, Vol. 3, Munich, Germany, 2015, pp. 234–241. doi:10.1007/978-3-319-24574-4_28.
- [16] S. Chopra, R. Hadsell, Y. LeCun, Learning a similarity metric discriminatively, with application to face verification, in: 2005 IEEE Computer Society Conference on Computer Vision and Pattern Recognition (CVPR’05), Vol. 1, IEEE, San Diego, California, United States of America, 2005, pp. 539–546. doi:10.1109/CVPR.2005.202.
- [17] H. Oh Song, Y. Xiang, S. Jegelka, S. Savarese, Deep metric learning via lifted structured feature embedding, in: 2016 IEEE Conference on Computer Vision and Pattern Recognition (CVPR), Las Vegas, Nevada, United States of America, 2016, pp. 4004–4012. doi:10.1109/CVPR.2016.434.
- [18] K. He, X. Zhang, S. Ren, J. Sun, Deep residual learning for image recognition, in: 2016 IEEE Conference on Computer Vision and Pattern Recognition (CVPR), Las Vegas, Nevada, United States of America, 2016, pp. 770–778. doi:10.1109/CVPR.2016.90.

- [19] J. Schlemper, O. Oktay, M. Schaap, M. Heinrich, B. Kainz, B. Glocker, D. Rueckert, Attention gated networks: Learning to leverage salient regions in medical images, *Medical Image Analysis* 53 (2019) 197–207. doi:10.1016/j.media.2019.01.012.
- [20] H. Cao, Y. Wang, J. Chen, D. Jiang, X. Zhang, Q. Tian, M. Wang, Swin-Unet: Unet-like pure transformer for medical image segmentation, in: *Computer Vision – ECCV 2022 Workshops*, Vol. 3, Tel Aviv, Israel, 2023, pp. 205–218. doi:10.1007/978-3-031-25066-8_9.
- [21] Z. Liu, Y. Lin, Y. Cao, H. Hu, Y. Wei, Z. Zhang, S. Lin, B. Guo, Swin Transformer: Hierarchical vision transformer using shifted windows, in: *2021 IEEE/CVF International Conference on Computer Vision (ICCV)*, Montreal, Quebec, Canada, 2021, pp. 9992–10002. doi:10.1109/ICCV48922.2021.00986.
- [22] A. M. Tahir, M. E. H. Chowdhury, A. Khandakar, T. Rahman, Y. Qiblawey, U. Khurshid, S. Kiranyaz, N. Ibtehaz, M. S. Rahman, S. Al-Maadeed, S. Mahmud, M. Ezeddin, K. Hameed, T. Hamid, COVID-19 infection localization and severity grading from chest X-ray images, *Computers in Biology and Medicine* 139 (2021) 105002. doi:10.1016/j.combiomed.2021.105002.
- [23] P. Porwal, S. Pachade, M. Kokare, G. Deshmukh, J. Son, W. Bae, L. Liu, J. Wang, X. Liu, L. Gao, T. Wu, J. Xiao, F. Wang, B. Yin, Y. Wang, G. Danala, L. He, Y. H. Choi, Y. C. Lee, S.-H. Jung, Z. Li, X. Sui, J. Wu, X. Li, T. Zhou, J. Toth, A. Baran, A. Kori, S. S. Chennamsetty, M. Safwan, V. Alex, X. Lyu, L. Cheng, Q. Chu, P. Li, X. Ji, S. Zhang, Y. Shen, L. Dai, O. Saha, R. Sathish, T. Melo, T. Araújo, B. Harangi, B. Sheng, R. Fang, D. Sheet, A. Hajdu, Y. Zheng, A. M. Mendonça, S. Zhang, A. Campilho, B. Zheng, D. Shen, L. Giancardo, G. Quéllec, F. Mériaudeau, IDRiD: Diabetic retinopathy – Segmentation and grading challenge, *Medical Image Analysis* 59 (2020) 101561. doi:10.1016/j.media.2019.101561.
- [24] D. P. Kingma, J. Ba, Adam: A method for stochastic optimization, in: *3rd International Conference on Learning Representations*, San Diego, California, United States of America, 2015.

- [25] I. Loshchilov, F. Hutter, SGDR: Stochastic gradient descent with warm restarts, in: 5th International Conference on Learning Representations, Vol. 1, Toulon, France, 2017, pp. 1769–1784.
- [26] P. Goyal, P. Dollár, R. Girshick, P. Noordhuis, L. Wesolowski, A. Kyrola, A. Tulloch, Y. Jia, K. He, Accurate, large minibatch SGD: Training ImageNet in 1 hour (June 2018). [arXiv:1706.02677v2](#).
- [27] I. Loshchilov, F. Hutter, Decoupled weight decay regularization, in: 7th International Conference on Learning Representations, New Orleans, Louisiana, United States of America, 2019.
- [28] C. Szegedy, V. Vanhoucke, S. Ioffe, J. Shlens, Z. Wojna, Rethinking the Inception architecture for computer vision, in: 2016 IEEE Conference on Computer Vision and Pattern Recognition (CVPR), Las Vegas, Nevada, United States of America, 2016, pp. 2818–2826. doi:10.1109/CVPR.2016.308.
- [29] G. Huang, Y. Sun, Z. Liu, D. Sedra, K. Q. Weinberger, Deep networks with stochastic depth, in: Computer Vision – ECCV 2016, Vol. 4, Amsterdam, The Netherlands, 2016, pp. 646–661. doi:10.1007/978-3-319-46493-0_39.
- [30] H. Touvron, M. Cord, M. Douze, F. Massa, A. Sablayrolles, H. Jegou, Training data-efficient image transformers & distillation through attention, in: Proceedings of the 38th International Conference on Machine Learning, Proceedings of Machine Learning Research, 2021, pp. 10347–10357.
- [31] Z. Liu, H. Mao, C.-Y. Wu, C. Feichtenhofer, T. Darrell, S. Xie, A ConvNet for the 2020s, in: 2022 IEEE/CVF Conference on Computer Vision and Pattern Recognition (CVPR), New Orleans, Louisiana, United States of America, 2022, pp. 11976–11986. doi:10.1109/CVPR52688.2022.01167.
- [32] E. D. Cubuk, B. Zoph, J. Shlens, Q. V. Le, RandAugment: Practical automated data augmentation with a reduced search space, in: 2020 IEEE/CVF Conference on Computer Vision and Pattern Recognition Workshops (CVPRW), Seattle, Washington, United States of America, 2020, pp. 3008–3017. doi:10.1109/CVPRW50498.2020.00359.

- [33] H. Zhang, M. Cisse, Y. N. Dauphin, D. Lopez-Paz, mixup: Beyond empirical risk minimization, in: 6th International Conference on Learning Representations, Vancouver, British Columbia, Canada, 2018.
- [34] S. Yun, D. Han, S. Chun, S. J. Oh, Y. Yoo, J. Choe, CutMix: Regularization strategy to train strong classifiers with localizable features, in: 2019 IEEE/CVF International Conference on Computer Vision (ICCV), Seoul, South Korea, 2019, pp. 6022–6031. doi:10.1109/ICCV.2019.00612.
- [35] Z. Zhong, L. Zheng, G. Kang, S. Li, Y. Yang, Random erasing data augmentation, in: Proceedings of the AAAI Conference on Artificial Intelligence, Vol. 34, New York, New York, United States of America, 2020, pp. 13001–13008. doi:10.1609/aaai.v34i07.7000.
- [36] C. H. Sudre, W. Li, T. Vercauteren, S. Ourselin, M. Jorge Cardoso, Generalised Dice overlap as a deep learning loss function for highly unbalanced segmentations, in: Deep Learning in Medical Image Analysis and Multimodal Learning for Clinical Decision Support, Québec City, Quebec, Canada, 2017, pp. 240–248. doi:10.1007/978-3-319-67558-9_28.

Appendix A. Implementation Details

Appendix A.1. Model Architectures

Appendix A.1.1. U-Net

The original model architecture [15] was implemented, with slight modifications. At the beginning of the model, a 3×3 convolutional layer is added, transforming the input to 64 channels. The five encoder and four decoder levels follow, each consisting of two 3×3 convolutions. The number of channels at the end of the levels are 64, 128, 256, 512, and finally 1024 at the bottom level. Padding is applied to all convolutional layers, so the full model preserves the spatial size of its input.

Appendix A.1.2. ResNet50 Attention U-Net

A standard ResNet50 was used as encoder, following the original architecture [18]. Bias was omitted in its convolutional layers, and stochastic depth with a rate of 0.1 was applied.

The decoder had five levels, with 256, 128, 64, 32, and 16 channels respectively, and a standard two-convolution block in each level. Through the lateral connections, the output of each level of the ResNet50 (including the output of its first 7×7 convolution) was connected to the decoder. This results in a total of four lateral skip connections. The final decoder level received no skip connections.

The attention gates in the lateral skip connections were identical to that of Attention U-Net [19].

Appendix A.1.3. Swin U-Net

Our implementation of Swin U-Net followed the original architecture [20] closely. It was trained with a stochastic depth of rate 0.2.

Appendix A.1.4. Weight initialization

The weights of U-Net and ResNet50 Attention U-Net were initialized in the same manner. Weights of convolutional layers were initialized according to He’s initialization scheme, that is, from $\mathcal{N}(0, \sigma^2)$, where

$$\sigma = \sqrt{\frac{\gamma}{\delta}}, \quad (\text{A.1})$$

where δ is the number of input neurons, and $\gamma = 2$.

In the case of Swin U-Net, the patch embedding and final patch expanding layers were initialized similarly, but with $\gamma = \frac{1}{3}$. The rest of the layers in this model were initialized from a truncated normal distribution with 0 mean, 0.02 standard deviation, and values not from $[-2, 2]$ resampled.

Biases were initialized to 0, and normalization layers were initialized to 0 mean and unit variance.

Appendix A.2. Datasets and Preprocessing

The ACDC and COVID-QU frames all have sizes of 256×256 , whose channels were then multiplied to match the 3 channel input format required by our segmentation models. Images from these datasets were resized to 224×224 using bilinear interpolation.

For training on IDRiD, the original images were first resized to 1120×2240 , then slices were taken from these by sliding a 448×448 window over the image, with a stride of 112. Figure A.1 shows one preprocessed image, along with its segmentation mask, from each dataset.

To the best of our knowledge, all data was collected and used responsibly.

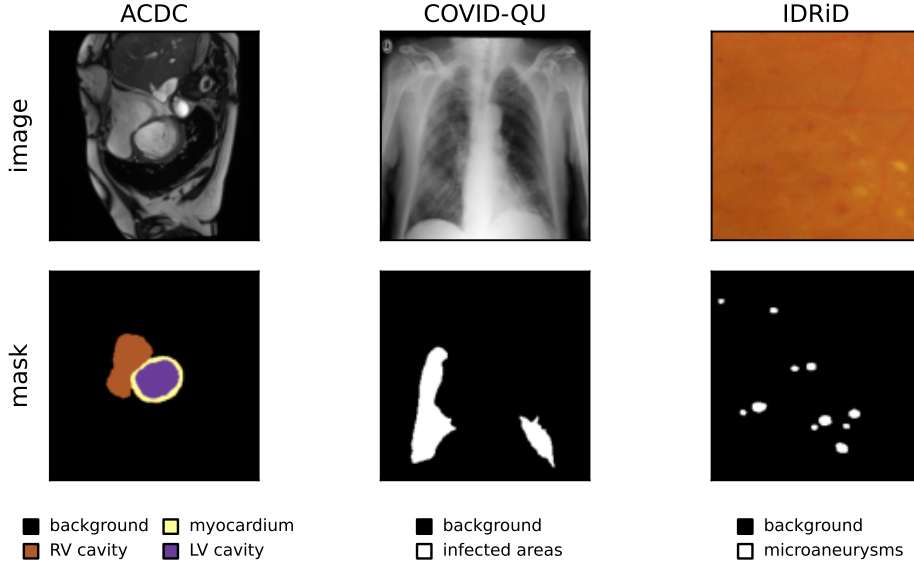


Figure A.1: An example image and its segmentation mask from each dataset

	simple scheme	advanced scheme
batch size	4096	4096 for convnets 1024 for Swin Transformer
base learning rate	0.004	$0.001 \cdot \frac{\text{batch size}}{1024}$
warmup length	20 for U-Net 5 for other models	20
augmentation	random flip	RandAugment, mixup, CutMix, random erasing

Table A.1: Hyperparameters used in the two pretraining schemes

Appendix A.3. Pretraining Methods

During ImageNet pretraining, the encoder architectures were extended with a classification head. The output of the encoder were pooled along the spatial axes, and then a one-layer dense classification head with a softmax activation function was added to predict class probabilities. As for loss function, the standard categorical cross entropy was used, with a label smoothing coefficient of 0.1. The Adam optimizer was applied, with hyperparameters $\beta_1 = 0.9$, $\beta_2 = 0.999$, and decoupled weight decay of 0.05.

Table A.1 details the differences between simple and advanced pretraining. The pseudocode for the augmentation is described in Algorithm 1. Label smoothing is applied after mixup or CutMix changes. For validation, images were resized so their shorter side would be 224, and then center crop was applied.

Algorithm 1 Augmenting images for ImageNet pretrainig

Input: image, label

$A \sim \mathcal{U}([0.8, 1])$ \triangleright sample uniform random number
crop rectangle from image with relative area A
resize rectangle to 224×224

$\omega \sim \mathcal{U}(\{0, 1\})$ \triangleright sample uniform random bit
if ω **then**
 apply horizontal flip
end if

if advanced pretraining **then**
 RandAugment(image)

$\xi \sim \mathcal{U}([0, 1])$
if $\xi \leq 0.9$ **then**
 sample an (image₂, label₂) pair uniformly from the whole dataset
 if $\xi \leq 0.5$ **then**
 CutMix(image, image₂, label, label₂)
 else
 mixup(image, image₂, label, label₂)
 end if
end if

$\psi \sim \mathcal{U}([0, 1])$
if $\psi \leq 0.25$ **then** \triangleright random erasing
 $S \sim \mathcal{U}([0.02, 0.33])$
 $r \sim \mathcal{U}([0.3, 3.3])$
 $h = \sqrt{Sr}$, $w = \sqrt{\frac{S}{r}}$
 randomly chosen area with relative size (h, w) is blackened out
end if

end if

return image, label

Appendix A.4. Downstream Training Methods

Segmentation models were trained for 150 epochs, with a batch size of 24, using SGD with a momentum of 0.9, and 0.0001 weight decay. A polynomial learning rate schedule was used, with exponent 0.9 and with base learning rate 0.05, meaning that the learning rate in the i^{th} iteration was $0.05 \cdot (1 - \frac{i}{N})^{0.9}$, where N is the total number of iterations.

For a batch of predicted masks $\hat{y} \in [0, 1]^{B \times H \times W \times (C+1)}$ and ground truth masks $y \in \{0, 1\}^{B \times H \times W \times (C+1)}$ (where B is the batch size, C is the number of non-background classes, and $H \times W$ is the spatial size of the images), the Dice loss is calculated as

$$\mathcal{L}_{\text{Dice}}(\hat{y}, y) = 1 - \frac{1}{C+1} \sum_{c=0}^C \frac{2 \cdot \langle \hat{y}_{\cdot, c}, y_{\cdot, c} \rangle + \zeta}{\|\hat{y}_{\cdot, c}\|^2 + \|y_{\cdot, c}\|^2 + \zeta}, \quad (\text{A.2})$$

where $\zeta = 10^{-5}$ is a smoothing term, $y_{b, h, w, c} = 1$ if and only if the pixel at position (h, w) in image b of the batch belongs to class c , and $\hat{y}_{b, h, w, c}$ describes the probability of pixel (h, w) of image b belonging to class c . In the case of multiclass segmentation, $\hat{y}_{\cdot, c}$ is obtained as the c^{th} coordinate of the softmaxed intensities of the output of the model. In the case of binary classification, a pixelwise sigmoid is applied to the output of the model, which is understood as the probability of the positive class; the probability of the negative class is then calculated in the natural manner.

During training, images from ACDC and COVID-QU were augmented by applying a random rotation (with angle sampled uniformly from $[0, \pi]$) and random vertical flip (with probability 0.5). Algorithm 2 describes the augmentation scheme for IDRiD. (See Algorithm 3 for details of color jittering.)

Appendix A.5. Downstream Evaluation Metrics

In the case of multiclass segmentation, the class with the highest probability is considered as the prediction. In binary tasks, pixels with intensity above 0.5 (after applying sigmoid) are considered to be predicted as positive.

Dice index was used to evaluate downstream performance. The Dice index associated with one class was calculated as

$$m_{\text{Dice}, c} = \frac{2 \cdot \text{TP}_c + 1}{2 \cdot \text{TP}_c + \text{FP}_c + \text{FN}_c + 1}, \quad (\text{A.3})$$

where TP_c , FP_c , and FN_c are the number of true positives, false positives, and false negatives for class c , respectively. (The 1s are added to the numerator

Algorithm 2 Augmenting images for training on IDRiD

Input: image, mask (448×448)

$\varphi \sim \mathcal{U}([0, 2\pi))$

rotate by φ \triangleright rotated image is padded; new side lengths are $448(\sin \varphi + \cos \varphi)$

$h_0 = 224 \cos \varphi \sin \varphi$

$w_0 = (448 - 224 \cos \varphi) \cos \varphi$

$\ell = 448 - 224(\sin \varphi + \cos \varphi)$

$h \sim \mathcal{U}([h_0, h_0 + \ell])$

$w \sim \mathcal{U}([w_0, w_0 + \ell])$

crop a 224×224 image, with top left coordinates (h, w)

$\omega \sim \mathcal{U}(\{0, 1\})$

if ω **then**

apply vertical flip

end if

ColorJitter(image)

return image, mask

and denominator for numerical stability.) For binary segmentation tasks, $m_{\text{Dice},1}$ is taken. For multiclass tasks, the Dice indices are averaged over all non-background classes.

We note that other metrics are sometimes used to evaluate semantic segmentation tasks. However, some of them, such as accuracy, specificity (true negative rate), and the area under the ROC curve are not suitable for datasets with label imbalance, which is present in the datasets used in this paper. In contrast, metrics like modified Hausdorff distance¹, the area under the precision–recall curve (mean average precision, or mAP), the Matthews cor-

¹Since Equation 1 requires maximization, the inverse of this should be taken for TIS calculation, which we denote with $-\text{HD95}$.

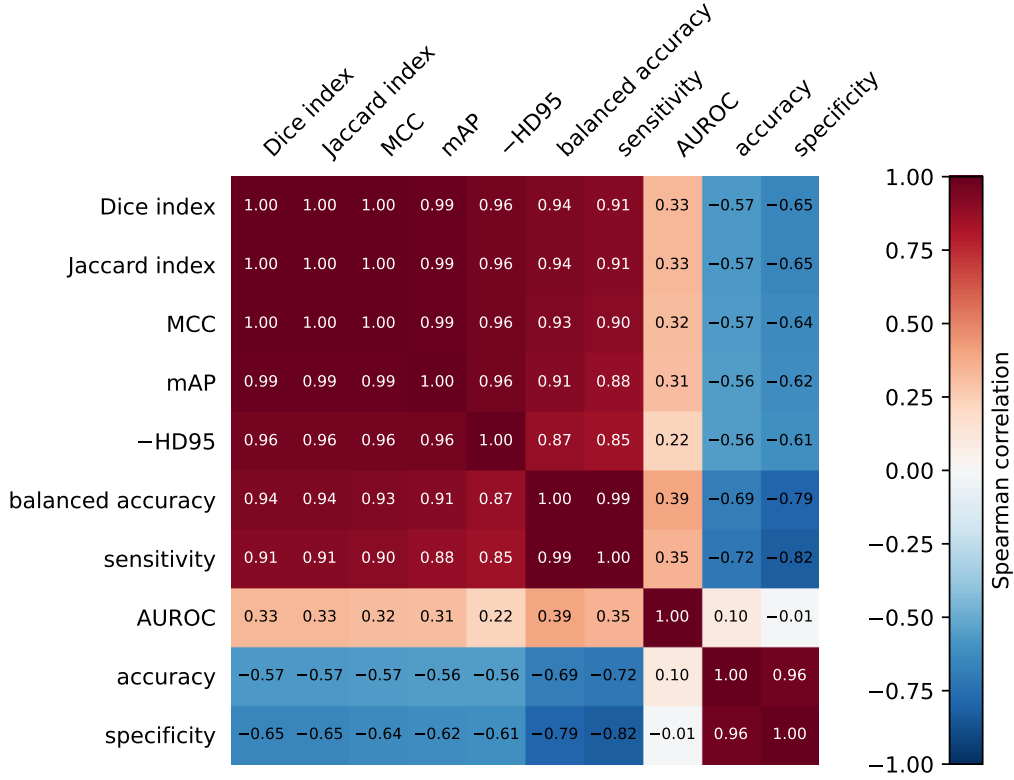


Figure A.2: Spearman correlation of different segmentation evaluation metrics

relation coefficient (MCC), and the Jaccard index handle unbalanced datasets well, and several of them (or their variants) have been utilized to evaluate performance on the datasets used in this paper.

We chose not to report transferability indicator scores calculated based on these metrics. This was done both for the sake of simplicity and because we found that they all highly correlated with each other, and therefore were likely to produce very similar (if not identical) TIS. Figure A.2 shows the Spearman correlation values of all considered metrics, calculated over the performances of more than 1000 models. -HD95, mAP, MCC, Jaccard and Dice indices all show an over 96% correlation with each other.

Our GitHub repository contains a table with model performances in all metrics.

Appendix A.6. Calculating Robustness

For each training configuration, nine pretraining checkpoints – after epochs 1, 5, 20, 50, 100, 150, 200, 250, and 300 – were taken, along with a randomly initialized model, to measure robustness. Each image was augmented twice, according to Algorithm 3. The first augmented version was used as the query \tilde{q} . The second version was used as the positive key k^+ for that query, and also as the negative key k^- for another image. This way, calculating the robustness of one encoder checkpoint required running a forward pass for each image twice.

For each checkpoint, the associated downstream performance was calculated as the mean of five runs. Transferability indicator scores were obtained by comparing these mean values.

Algorithm 3 ColorJitter

Input: $x \in [0, 1]^{H \times W \times 3}$ image

$\lambda_b \sim \mathcal{U}([0.9, 1.1])$ ▷ brightness jitter
 $x = \lambda_b x$

$w = (0.2989, 0.587, 0.114)$
 $\bar{x} = \sum_{c=1}^3 w_c x_{\cdot, c}$ ▷ convert x to grayscale; weighting channels by w

$\lambda_c \sim \mathcal{U}([0.95, 1.05])$ ▷ contrast jitter
 $\mu = \frac{1}{HW} \sum_{h,w} \bar{x}_{h,w}$
 $x = \lambda_c x + (1 - \lambda_c) \mu$

$\lambda_s \sim \mathcal{U}([0.9, 1.1])$ ▷ saturation jitter
 $x = \lambda_s x + (1 - \lambda_s) \bar{x}$

$x = \text{HSV}(x)$ ▷ transform from RGB to HSV (hue–saturation–value space)

$\lambda_h \sim \mathcal{U}([-0.05, 0.05])$ ▷ hue jitter
 $x_{\cdot, 1} = x_{\cdot, 1} + \lambda_h \pmod{1}$ ▷ first channel of HSV is hue

$x = \text{RGB}(x)$ ▷ transform from HSV to RGB

return x

Appendix A.7. Software and Hardware Details

Our experiments were conducted on a computer utilizing $2\times$ Intel Xeon Gold 5320 CPU @ 2.20GHz (52 threads each), $8\times$ NVIDIA A100-SXM4-80GB GPU, and 2 TB RAM. The models and the experiment framework are implemented using PyTorch, running on an Ubuntu 22.04.4 LTS operating system. The exact list of required packages is available in the GitHub repository.

Appendix B. Results in More Detail

This section provides the TIS of our method, as well as its variants, described in Section 7. Tables B.1–B.3 list the detailed results for each configuration. When a parameter (encoder level, pooling, distance metric, or margin) is not indicated, it was set as described in Section 6. The figures of the final method – that of cosine distance with a margin of 0.5 – are outlined with a black frame.

Robustness scores for each encoder checkpoint can be found in our GitHub repository.

		basic U-Net		R50 Atn. U-Net		Swin U-Net	
		full training	decoder only	full training	decoder only	full training	decoder only
ImageNet accuracy		0.999	0.987	1.000	0.998	1.000	0.997
no pretraining		1.000	0.978	0.992	0.939	0.905	0.818
level	pooled						
last	yes	0.994	1.000	0.999	1.000	0.905	0.818
	no	0.997	0.995	0.999	1.000	0.998	1.000
second to last	yes	0.992	0.998	0.999	1.000	0.998	0.997
	no	0.996	0.990	0.999	1.000	0.998	1.000
metric	margin						
correlation	0.50	0.996	0.998	0.992	0.936	0.998	0.818
L^2 distance		0.992	0.981	0.995	0.971	0.956	0.948
cosine distance	0.25	0.996	0.998	0.999	1.000	0.998	0.967
	0.50	0.996	0.998	0.999	1.000	0.998	0.997
	0.75	0.996	0.998	0.999	1.000	0.998	0.997
	1.00	0.996	0.998	0.999	1.000	0.998	0.997

(a) Simple pretraining

		basic U-Net		R50 Atn. U-Net		Swin U-Net	
		full training	decoder only	full training	decoder only	full training	decoder only
ImageNet accuracy		1.000	0.975	0.992	0.940	0.902	0.801
no pretraining		0.996	0.977	0.992	0.936	0.952	0.808
level	pooled						
last	yes	0.996	0.977	1.000	0.999	0.998	0.987
	no	0.996	0.977	1.000	0.999	1.000	0.980
second to last	yes	0.996	1.000	1.000	0.999	0.999	1.000
	no	0.996	0.994	0.992	0.975	0.952	0.808
metric	margin						
correlation	0.50	0.996	1.000	0.992	0.999	0.952	0.980
L^2 distance		0.997	0.998	0.996	0.997	0.952	0.989
cosine distance	0.25	0.996	1.000	0.992	0.999	1.000	1.000
	0.50	0.996	1.000	0.992	0.999	0.952	1.000
	0.75	0.996	1.000	0.992	0.999	0.952	1.000
	1.00	0.996	1.000	0.992	0.999	0.952	1.000

(b) Advanced pretraining

Table B.1: Detailed results on ACDC

		basic U-Net		R50 Atn. U-Net		Swin U-Net	
		full training	decoder only	full training	decoder only	full training	decoder only
ImageNet accuracy		0.998	0.976	1.000	0.999	0.998	1.000
no pretraining		1.000	0.962	0.980	0.923	0.920	0.859
level	pooled						
last	yes	0.990	0.973	0.993	1.000	0.975	0.943
	no	0.990	0.973	0.993	1.000	0.975	0.943
second to last	yes	0.997	0.979	1.000	0.999	0.988	0.970
	no	0.998	0.976	0.993	0.995	1.000	0.998
metric	margin						
correlation	0.50	1.000	0.985	0.993	0.928	1.000	0.943
L^2 distance		1.000	0.990	0.989	0.928	0.975	0.925
cosine distance	0.25	1.000	0.985	0.993	0.997	1.000	0.988
	0.50	1.000	0.985	0.993	0.995	1.000	0.988
	0.75	1.000	0.985	0.993	0.995	1.000	0.988
	1.00	1.000	0.985	0.993	0.995	1.000	0.988

(a) Simple pretraining

		basic U-Net		R50 Atn. U-Net		Swin U-Net	
		full training	decoder only	full training	decoder only	full training	decoder only
ImageNet accuracy		0.999	0.968	0.980	0.922	0.919	0.854
no pretraining		1.000	0.984	0.980	0.927	0.919	0.872
level	pooled						
last	yes	0.997	0.985	0.995	0.996	0.990	1.000
	no	1.000	0.980	0.996	0.995	1.000	0.985
second to last	yes	1.000	0.980	0.995	0.996	0.989	0.993
	no	0.999	0.968	0.996	0.995	0.990	1.000
metric	margin						
correlation	0.50	0.999	0.985	0.980	0.955	0.990	0.993
L^2 distance		0.993	0.999	0.992	0.955	0.993	0.980
cosine distance	0.25	0.999	0.985	0.980	0.996	0.990	0.993
	0.50	0.999	0.980	0.996	0.996	0.990	0.993
	0.75	0.999	0.997	0.980	0.996	0.919	0.993
	1.00	0.999	0.997	0.980	0.996	0.919	0.993

(b) Advanced pretraining

Table B.2: Detailed results on COVID-QU

		basic U-Net		R50 Atn. U-Net		Swin U-Net	
		full training	decoder only	full training	decoder only	full training	decoder only
ImageNet accuracy		1.000	0.997	0.973	0.999	1.000	1.000
no pretraining		0.981	0.906	0.994	0.925	0.830	0.740
level	pooled						
last	yes	0.941	0.969	0.949	0.988	0.830	0.740
	no	0.999	1.000	0.994	0.925	0.830	0.740
second to last	yes	0.941	0.969	0.935	1.000	0.994	0.970
	no	0.999	1.000	0.960	0.972	1.000	0.998
metric	margin						
correlation	0.50	0.981	0.947	0.960	0.925	1.000	0.938
L^2 distance		0.963	0.967	0.978	0.932	0.830	0.909
cosine distance	0.25	0.981	0.995	0.994	0.925	0.830	0.938
	0.50	0.999	0.969	0.960	1.000	1.000	0.970
	0.75	0.981	0.995	0.927	0.925	1.000	0.745
	1.00	0.981	0.995	0.927	0.925	1.000	0.745

(a) Simple pretraining

		basic U-Net		R50 Atn. U-Net		Swin U-Net	
		full training	decoder only	full training	decoder only	full training	decoder only
ImageNet accuracy		0.992	0.910	0.991	0.924	0.824	0.748
no pretraining		0.986	0.941	1.000	0.926	0.877	0.758
level	pooled						
last	yes	0.984	0.991	1.000	0.926	0.993	0.993
	no	0.986	0.941	1.000	0.926	0.999	0.990
second to last	yes	0.984	0.991	0.938	0.983	0.993	0.993
	no	0.986	0.941	1.000	0.926	0.999	0.990
metric	margin						
correlation	0.50	0.986	0.969	0.941	0.983	0.999	0.929
L^2 distance		0.943	0.977	0.938	0.953	0.965	0.975
cosine distance	0.25	0.986	1.000	1.000	0.983	0.965	0.993
	0.50	0.986	0.991	1.000	0.983	0.999	0.993
	0.75	0.986	1.000	0.938	0.983	0.999	0.993
	1.00	0.986	1.000	0.938	0.983	0.999	0.993

(b) Advanced pretraining

Table B.3: Detailed results on IDRiD